Northumbria Research Link

Citation: Qiu, Shi, Yuan, Jinhui, Zhou, Xian, Qu, Yuwei, Yan, Binbin, Wu, Qiang, Wang, Kuiru, Sang, Xinzhu, Long, Keping and Yu, Chongxiu (2020) Highly sensitive temperature sensing based on all-solid cladding dual-core photonic crystal fiber filled with the toluene and ethanol. Optics Communications, 477. p. 126357. ISSN 0030-4018

Published by: Elsevier

URL: https://doi.org/10.1016/j.optcom.2020.126357 <https://doi.org/10.1016/j.optcom.2020.126357>

This version was downloaded from Northumbria Research Link: http://nrl.northumbria.ac.uk/id/eprint/45173/

Northumbria University has developed Northumbria Research Link (NRL) to enable users to access the University's research output. Copyright © and moral rights for items on NRL are retained by the individual author(s) and/or other copyright owners. Single copies of full items can be reproduced, displayed or performed, and given to third parties in any format or medium for personal research or study, educational, or not-for-profit purposes without prior permission or charge, provided the authors, title and full bibliographic details are given, as well as a hyperlink and/or URL to the original metadata page. The content must not be changed in any way. Full items must not be sold commercially in any format or medium without formal permission of the copyright holder. The full policy is available online: http://nrl.northumbria.ac.uk/policies.html

This document may differ from the final, published version of the research and has been made available online in accordance with publisher policies. To read and/or cite from the published version of the research, please visit the publisher's website (a subscription may be required.)

Northumbria University NEWCASTLE

University Library

Highly sensitive temperature sensing based on all-solid cladding dual-core photonic crystal fiber filled with the toluene and ethanol

Shi Qiu[a)] Jinhui Yuan[a)b)*] Xian Zhou[b)] Yuwei Qu [a)] Binbin Yan[a)] Qiang Wu[c)d)*] Kuiru Wang[a)] Xinzhu Sang[a)] Keping Long[b)] Chongxiu Yu[a)]

[a] *State Key Laboratory of Information Photonics and Optical Communications, Beijing University of Posts and Telecommunications, Beijing 100876, China*

[b] *Research Center for Convergence Networks and Ubiquitous Services, University of Science & Technology Beijing (USTB), Beijing 100083, China*

[c] *Department of Physics and Electrical Engineering, Northumbria University, Newcastle upon Tyne, NE1 8ST, United Kingdom*

[d] *Key Laboratory of Nondestructive Test (Ministry of Education), Nanchang Hong Kong University, Nanchang 330063, China*

**yuanjinhui81@bupt.edu.cn; qiang.wu@northumbria.ac.uk*

Abstract An all-solid cladding dual-core photonic crystal fiber (DC-PCF) filled with toluene and ethanol is proposed for the temperature sensing. The all-solid cladding is formed by using the fluorine-doped silica glass instead of the air holes in the cladding region. By selectively filling the toluene and ethanol into the three air holes near the core region, the characteristic of the temperature sensing is numerically investigated. The simulation results show that the average sensitivity of the temperature sensing can achieve -11.64 and -7.41 nm/℃ in the temperature ranges from 0 to 70 ℃ and -80 to 0 ℃, respectively, when the length of the DC-PCF is as short as 1.6 mm. The maximum sensitivity in the considered temperature ranges can be up to -15 and -9 nm/℃, respectively. Moreover, the proposed temperature sensor is insensitive to the hydrostatic pressure.

Keywords：Photonic crystal fiber; Temperature sensor; All-solid cladding; Finite element method;

1. Introduction

Photonic crystal fiber (PCF) has important application in the development of novel optical devices due to its designable structure and unique optical characteristics, including adjustable dispersion, large mode field area, high birefringence, etc. In recent years, the sensing based on the PCFs has become a research hotspot [1-4]. At present, different kinds of PCF-based sensing have been reported, such as temperature sensing [1], refractive index sensing [2], magnetic sensing [3], pressure sensing [4], and so on. Among them, the temperature sensing has been attracting great research interests since it plays essential roles in the fields of medical testing, aerospace exploration, and food industry.

The PCF-based temperature sensing can be achieved by utilizing the liquid filling. As the PCF fabrication and multi-step infiltration technologies are developed [5], different sensing liquids, including toluene [6], ethanol [7], and liquid crystal [8], have been successfully filled into the PCFs. In 2016, Dong *et al* reported an ethanol-filled band-gap PCF for the temperature sensing [9]. In 2017, Ma *et al* demonstrated a toluene-filled PCF for the temperature sensing, where the average sensitivity can achieve -6.02 nm/℃ [10]. In 2019, Geng *et al* proposed a compact oil-filled PCF for the temperature sensing based on the four-wave mixing effect, where the average sensitivity is 0.61 nm/℃ in the detection range

of 30 to 150 ℃ [11]. In 2019, Mirza *et al* investigated a water-filled dual-core PCF (DC-PCF) for the temperature sensing, where the maximum sensitivity is 818 pm/℃ in the detection range of 30 to 70 ℃ [12]. In addition, the PCFs based on the surface plasmon resonance (SPR) effect can also be applied to the temperature sensing. In 2012, Peng *et al* reported a PCF-based temperature sensor, which was realized by selectively coating the gold film in the six air holes of the PCF [13]. In 2016, Liu *et al* achieved a PCF-based temperature-sensitive sensor by filling the liquid into the gold-coated air holes, where the average temperature sensitivity was −3.08 nm/℃ in the temperature range of 0 to 100 ℃ [14]. In 2017, Weng *et al* proposed a D-shaped liquid-filled PCF based on the SPR effect for the temperature sensing, where the average temperature sensitivity was −3.635 nm/℃ in the temperature range of 20 to 50 ℃ [15].

Recently, some investigations are concentrated on the all-solid cladding PCFs. Compared with the traditional air-silica PCFs, the all-solid cladding PCFs could avoid the deformation during drawing because other materials are used to take the place of the air holes in the cladding region. At present, different kinds of soft glasses are usually used as alternative materials in the design of the all-solid cladding PCFs [16, 17]. However, because of the large refractive index difference between the silica and soft glasses, their physical characteristics, including the transition temperature, viscosity coefficient, thermal expansion coefficient, have obvious difference. Thus, it is a great challenge to fabricate the soft glasses-based all-solid cladding PCFs in practice.

In this paper, we proposed an all-solid cladding DC-PCF filled with the toluene and ethanol for the temperature sensing. The all-solid cladding is formed by the fluorine-doped silica glass, and the refractive index difference between the fluorine-doped silica glass and silica is as low as -0.008. The temperature sensing performance of the proposed all-solid cladding DC-PCF is numerically investigated by the finite element method (FEM). The simulation results show that the average sensitivity can achieve -11.64 nm/℃ in the temperature range of 0 to 70 ℃ and -7.41 nm/℃ in the temperature range of -80 to 0 ℃, respectively. It is also demonstrated that the proposed temperature sensor based on the all-solid cladding DC-PCF is insensitive to the hydrostatic pressure.

2. Design of the all-solid cladding DC-PCF and theory

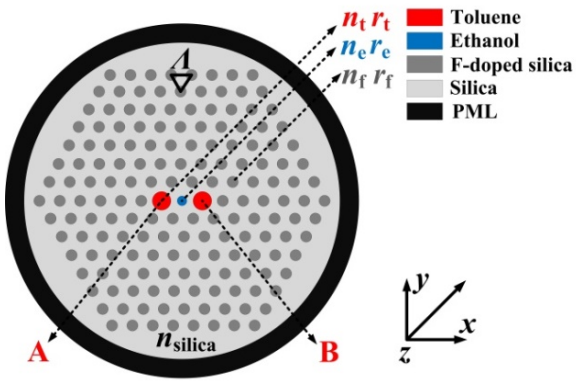

Fig. 1. The cross-sectional structure of the designed PCF.

Fig. 1 shows the cross-sectional structure of the designed all-solid cladding DC-PCF. The refractive index and radius of the fluorine-doped silica glass in the cladding region are set as n_f and r_f respectively. The cores A and B are formed by the two toluene-filled air holes, and the corresponding refractive index and radius are n_t and r_t, respectively. The central air hole is filled with the ethanol, and the refractive index and radius of the ethanol-filled air hole are set as n_e and r_e, respectively. The triangular lattice

constant is Λ, and the background material is the silica, whose refractive index is n_{silica}. It is worth indicating that n_f-n_{silica}= -0.008 is chosen. Compared with the conventional solid core PCF, the proposed all-solid cladding DC-PCF filled with the toluene and ethanol could achieve the better temperature sensing performances. The main reasons are considered as follows. First, the structure parameters of the all-solid cladding DC-PCF could be adjusted more flexible. Second, the thermal optical coefficient (3.94 $\times 10^{-4}$/°C) of the toluene and ethanol is the two orders of magnitude higher than that of the silica (8.6$\times 10^{-6}$/°C), which can significantly improve the temperature sensitivity. Third, the all-solid cladding is pressure resistant, and the liquids can be filled conveniently.

The FEM is used to calculate the propagation and temperature sensing characteristics of the proposed DC-PCF. In the simulation, the perfectly matched layer (PML) is added to the outermost layer of the PCF, and its thickness and refractive index are set as 15 μm and n_{silica}+0.03, respectively. In addition, the grid sizes of the silica, fluorine-doped silica, and PML are set as $\lambda/4$, and the grid size of the air holes filled with the toluene and ethanol is set as $\lambda/6$.

According to the coupled mode theory (CMT), the guiding modes of the DC-PCFs are called as the supermodes, which are formed by coupling the individual core mode in the same polarization direction. Figs. 2(a) and 2(b) show the mode field distributions of the even and odd supermodes in the *x*-polarized direction, respectively. Figs. 2(c) and 2(d) show the corresponding mode field distributions of the even and odd supermodes in the *y*-polarized direction, respectively.

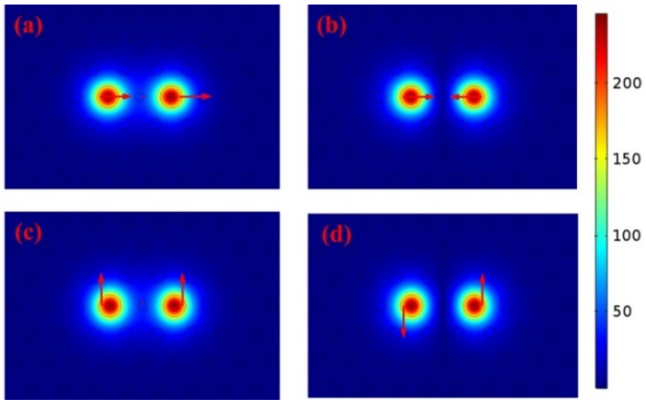

Fig. 2. The mode field distributions of the (a) *x*-polarized even supermode, (b) *x*-polarized odd supermode, (c) *y*-polarized even supermode, and (d) *y*-polarized odd supermode.

The refractive index of the silica n_{silica} can be obtained from Ref. [18]

$$n^2_{\text{silica}}(\lambda,T)=(1.31522+6.90754\times10^{-6}T)+\frac{(0.788404++23.5835\times10^{-6}T)\lambda^2}{\lambda^2-(0.0110199+0.584758\times10^{-6}T)}+\frac{(0.91316+0.548368\times10^{-6}T)\lambda^2}{\lambda^2-100}, \quad (1)$$

where T is the temperature in Celsius and λ is the free-space wavelength.

The refractive index of the toluene n_t can be calculated by the following equation [10]

$$n_t(\lambda)=1.474775+\frac{0.00690031}{\lambda^2}+\frac{2.1776\times10^{-4}}{\lambda^4}-\alpha(T-20.15). \quad (2)$$

The refractive index of the ethanol n_e can be described as [19, 20]

$$n_e(\lambda)=\sqrt{1+\frac{0.0165\lambda^2}{\lambda^2-9.08}-\frac{0.8268\lambda^2}{\lambda^2-0.01039}}-\alpha(T-20). \quad (3)$$

In Eqs. (2) and (3), the thermos optic coefficient α of the toluene and ethanol is chosen as α=3.94 $\times 10^{-4}$ /°C, which is the two orders of magnitude higher than that of the silica (8.6$\times 10^{-6}$ /°C) [21].

For the DC-PCFs, the coupling length L_c as an important parameter indicates that the maximum power transfers from the core A to B and can be described as [22, 23]

$$L_C^i = \frac{\lambda}{2(n^i_{\text{even}} - n^i_{\text{odd}})}, \qquad i=x,y \tag{4}$$

where n^i_{even} and n^i_{odd} represent the real parts of the effective refractive indices of the *i*-polarized even and odd supermodes, respectively.

If the input light is launched into the core A, the power transfers from the core A to B along the propagation direction can be described as [24, 25]

$$P_A = \cos^2(\frac{\pi}{2}\cdot\frac{L}{Lc}), \tag{5}$$

$$P_B = \sin^2(\frac{\pi}{2}\cdot\frac{L}{Lc}). \tag{6}$$

The temperature sensitivity is defined as [26, 27]

$$S(\text{nm/°C}) = \frac{\text{d}\lambda_{\text{peak}}}{\text{d}T}, \tag{7}$$

where $\text{d}\lambda_{\text{peak}}$ is the difference between the two peak wavelengths of the transmission curves and dT is the temperature change. By choosing the peak wavelength as the detection signal, it is possible to obtain the high signal to noise ratio [28].

3. Influences of the fiber structure parameters on the temperature sensing

In order to investigate the influences of the fiber structure parameters on the temperature sensing, the initial structure parameters are chosen as r_t=1.2 μm, Λ=3.5 μm, r_e=0.50 μm, and r_f=0.65 μm. The fiber length is set as L=1.5 mm. Moreover, the melting points of the toluene and ethanol are -94.9 and -114 °C, and the corresponding boiling points are 110.6 and 78°C, respectively. Therefore, considering the practical application and material characteristic, we set 0 °C as the boundary temperature, and then investigated the two temperature ranges of 0 to 70 °C and -80 to 0 °C, respectively.

According to Eq.(4), the two supermodes with the different polarization directions are orthogonal, and there is no coupling between them. Therefore, only the two supermodes in the same polarization direction can be used for the temperature sensing. For the proposed DC-PCF, the materials are isotropic, and the structure is regular hexagonal lattice, so the even and odd supermodes in the two polarization directions are degenerate, respectively. Thus, for the *x*-polarized and *y*-polarized supermodes, there is no difference between the temperature sensing results. In the following, only the *x*-polarized supermodes are chosen to investigate the temperature sensing.

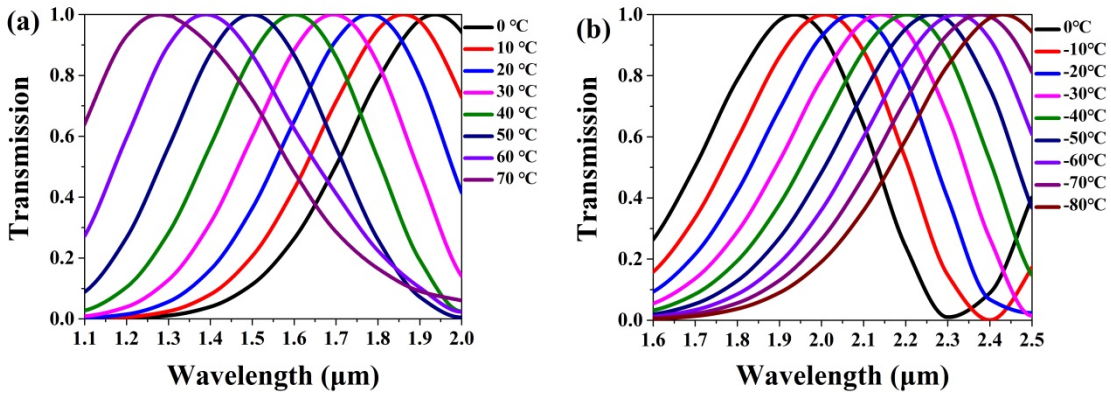

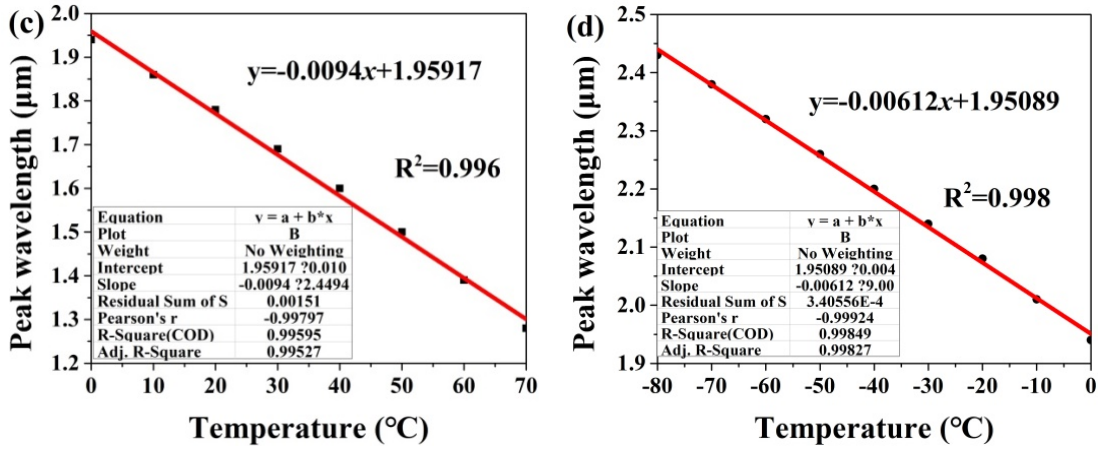

Fig. 3. The transmission spectra of the *x*-polarized light when the temperature changes from (a) 0 to 70 ℃ and (b) -80 to 0 ℃, respectively. The variation in the peak wavelengths and the linear fitting results when the temperature changes from (c) 0 to 70 ℃ and (d) -80 to 0 ℃, respectively.

Fig. 3(a) shows the transmission spectra of the *x*-polarized light in the temperature range of 0 to 70 ℃. According to Eq. (2), n_t decreases with the increase of the temperature. At this time, the evanescent field of the two cores becomes stronger, and the corresponding coupling effect is enhanced. Thus, as the temperature increases, the peak wavelengths occur to blue-shift. Fig. 3(b) shows the transmission spectra of the *x*-polarized light in the temperature range of -80 to 0 ℃. As the temperature decreases, the peak wavelength occurs to red-shift. Compared with the results shown in Fig. 3(a), the red-shift of the peak wavelengths becomes weak. The main reason is considered that n_t increases with the decrease of the temperature. Figs. 3(c) and 3(d) show the variations in the peak wavelengths and linear fitting results when the temperature changes from 0 to 70 ℃ and -80 to 0 ℃, respectively. From Fig. 3(c), the linear fitting result is y=-0.0094x+1.95917, R^2 is 0.996, the average sensitivity is -9.4 nm/℃, and the maximum sensitivity is 11.1 nm/℃in the temperature range of 60 to 70 ℃. According to Eqs. (2) and (3), α of the toluene and ethanol are the same, which means that the changes of n_t and n_e are the same when the temperature changes. Thus, the good linearity can be obtained for the temperature sensing. From Fig. 3(d), the linear fitting result is y=-0.00612x+1.95089, R^2 is 0.998, the average sensitivity is -6.12 nm/℃, and the maximum sensitivity is -7 nm/℃ in the temperature range of -20 to 0 ℃. Compared with Fig. 3(c), for the temperature range of -80 to 0 ℃, the average and maximum sensitivities are reduced, and R^2 remains basically the same due to the weakening evanescent field.

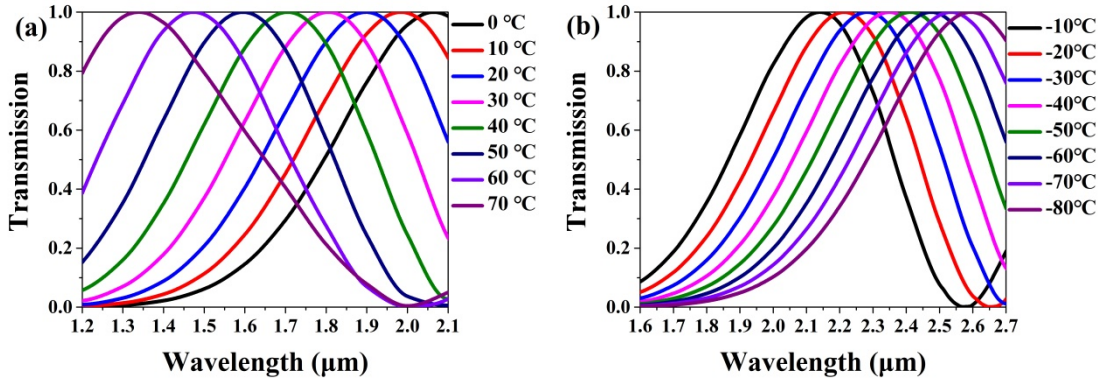

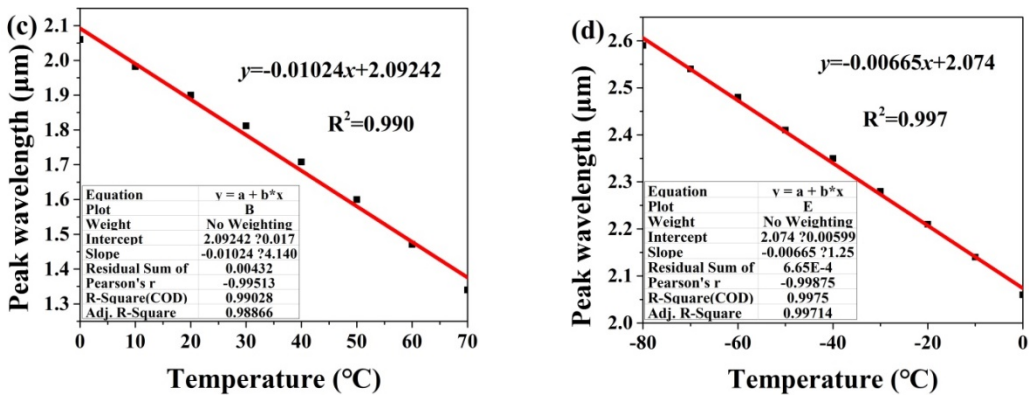

Fig. 4. The transmission spectra of the *x*-polarized light for the different temperature ranges from (a) 0 to 70 ℃ and (b) -80 to 0 ℃, respectively, when r_t=1.4 μm. The variations in the peak wavelengths and linear fitting results when the temperature changes from (c) 0 to 70 ℃ and (d) -80 to 0 ℃, respectively.

In the following, we will investigate the influences of the fiber structure parameters on the temperature sensing by changing r_t, Λ, r_e, and L, respectively. Fig. 4(a) shows the transmission spectra of the *x*-polarized light in the temperature range of 0 to 70 ℃ when r_t =1.4 μm. From Fig. 4(a), as the temperature increases, the peak wavelength occurs to blue-shift. Compared with the results of r_t=1.2 μm, the peak wavelengths at the same temperature occur to red-shift when r_t increases to 1.4 μm. The reason is considered that the increase of r_t weakens the evanescent field between the two cores. Fig. 4(b) shows the transmission spectra of the *x*-polarized light in the temperature range of -80 to 0 ℃ when r_t =1.4 μm. From Fig. 4(b), as the temperature decreases, the peak wavelengths occur to red-shift. Similar to the results shown in Fig. 4(a), the peak wavelengths at the same temperature also occur to red-shift. Figs. 4(c) and 4(d) show the variations in the peak wavelengths and linear fitting results when the temperature changes from 0 to 70 ℃ and -80 to 0 ℃, respectively. From Fig. 4(c), the linear fitting result is y=-0.01024x+2.09242, R^2 is 0.990, the average sensitivity is -10.24 nm/℃, and the maximum sensitivity can achieve -12.9 nm/℃ in the temperature range of 60 to 70 ℃. From Fig. 4(d), the linear fitting result is y=-0.00665x+2.074, R^2 is 0.997, the average sensitivity is -6.65 nm/℃, and the maximum sensitivity can achieve -8.3 nm/℃ in the temperature range of 0 to -10 ℃. It is found that the temperature sensitivity can be improved by increasing r_t.

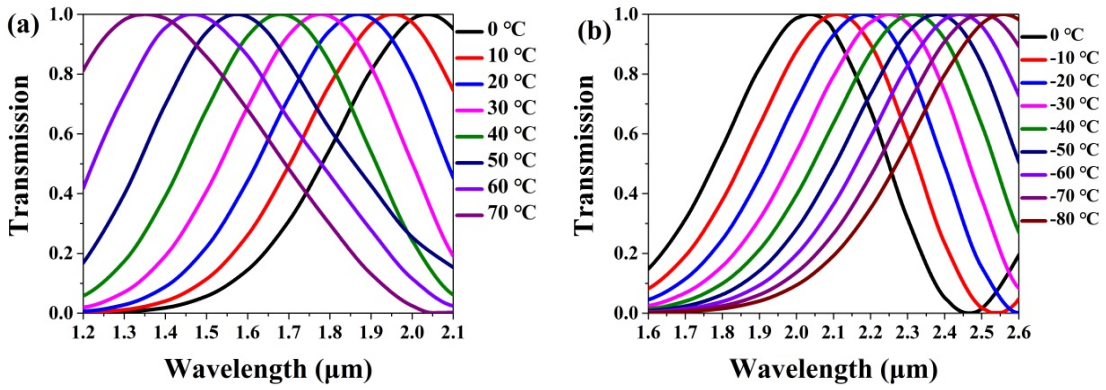

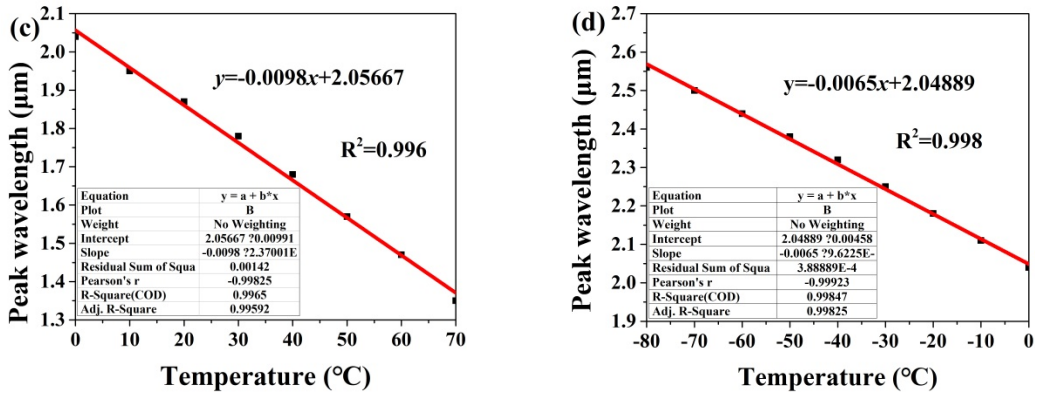

Fig. 5. The transmission spectra of the *x*-polarized light at different temperature ranges from (a) 0 to 70 ℃ and (b) -80 to 0 ℃, respectively, when Λ=3.7 μm. The variation in the peak wavelengths and linear fitting results when the temperature change from (c) 0 to 70 ℃ and (d) -80 to 0 ℃, respectively.

Fig. 5(a) shows the transmission spectra of the *x*-polarized light in the temperature range of 0 to 70 ℃ when Λ=3.7 μm. From Fig. 5(a), as the temperature increases, the peak wavelengths occur to blue-shift since the distance between the two cores increases as Λ increases. Compared with the results of Λ=3.5 μm, the peak wavelengths at the same temperature occur to red-shift when Λ increases to 3.7 μm. Fig. 5(b) shows the transmission spectra of the *x*-polarized light in the temperature range of -80 to 0 ℃ when Λ=3.7 μm. From Fig. 5(b), as the temperature decreases, the peak wavelengths occur to red-shift. Similar to the results shown in Fig. 5(a), when Λ increases from 3.5 to 3.7 μm, the peak wavelengths at the same temperature also occur to red-shift. Fig. 5(c) and 5(d) show the variation in the peak wavelengths and linear fitting results when the temperature changes from 0 to 70 ℃ and -80 to 0 ℃, respectively. From Fig. 5(c), the linear fitting result is y=-0.0098x+2.05667, R^2 is 0.996, the average sensitivity is -9.8 nm/℃, and the maximum sensitivity can achieve -12.0 nm/℃ in the temperature range of 60 to 70 ℃. From Fig. 5(d), the linear fitting result is y=-0.0065x+2.04889, R^2 is 0.998, the average sensitivity is -6.5 nm/℃, and the maximum sensitivity can achieve -7.1 nm/℃ in the temperature range of 0 to -30 ℃. Obviously, when Λ increases from 3.5 to 3.7 μm, the average sensitivity increases from -9.4 to -9.8 nm/℃ in the temperature range of 0 to 70 ℃ and -6.12 to -6.5 nm/℃ in the temperature range of -80 to 0 ℃, respectively.

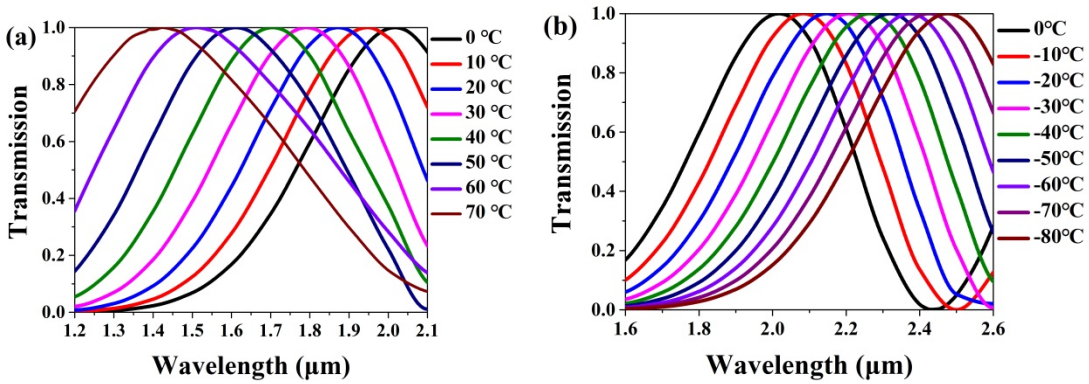

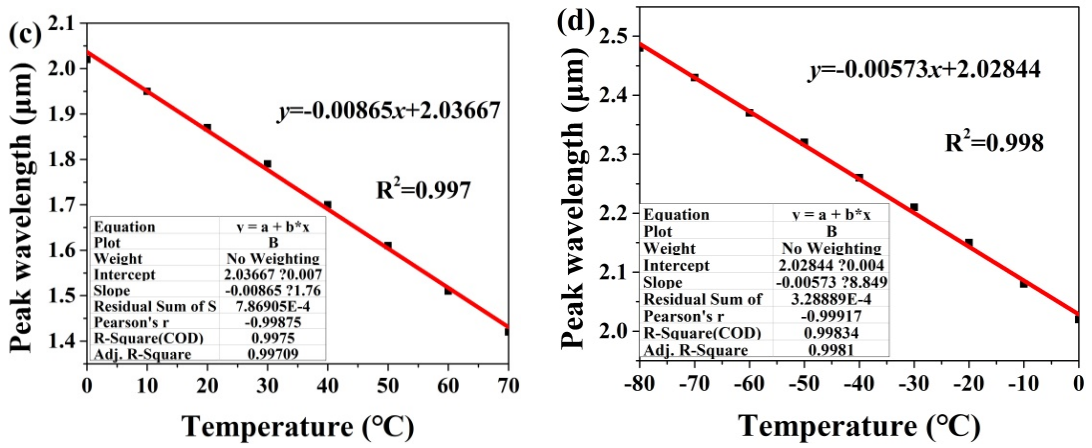

Fig. 6. The transmission spectra of the *x*-polarized light at different temperature ranges from (a) 0 to 70 ℃ and (b) -80 to 0 ℃, respectively, when r_e =0.7 μm; The variation in the peak wavelengths and linear fitting results when the temperature changes from (c) 0 to 70 ℃ and (d) -80 to 0 ℃, respectively.

Since the ethanol-filled air hole is located at the center of the coupling bridges between the two cores, r_e has also an important influence on the sensitivity. Except for r_t and Λ, the coupling effect can also be adjusted by the coupling bridge. Fig. 6(a) shows the transmission spectra of the *x*-polarized light in the temperature range of 0 to 70 ℃ when r_e =0.7 μm. From Fig. 6(a), as the temperature increases, the peak wavelengths occur to blue-shift. Because n_e is lower than n_{silica}, it can reduce the effective refractive index of the coupling bridge. Thus, compared with the results shown in Fig. 3(a), when r_e increases from 0.5 to 0.7 μm, the peak wavelengths at the same temperature occur to blue-shift. Fig. 6(b) shows the transmission spectra of the *x*-polarized light in the temperature range of -80 to 0 ℃ when r_e =0.7 μm. From Fig. 6(b), because the ethanol-filled air hole reduces the effective refractive index of the coupling bridge and n_t increases with the decrease of the temperature, the peak wavelengths at the same temperature also occur to red-shift. Figs. 6(c) and 6(d) show the variation in the peak wavelengths and linear fitting results when the temperature changes from 0 to 70 ℃ and -80 to 0 ℃, respectively. From Fig. 6(c), the linear fitting result is y=-0.00865x+2.03667, R^2 is 0.997, the average sensitivity is -8.65 nm/℃, and the maximum sensitivity can achieve -9.8 nm/℃ in the temperature range of 60 to 70 ℃. From Fig. 6(d), the linear fitting result is y=-0.00573x+2.02844, R^2 is 0.998, the average sensitivity is -5.73 nm/℃, and the maximum sensitivity can achieve -7.0 nm/℃ in the temperature range of 0 to -20 ℃. When r_e is increased from 0.5 to 0.7 μm, the average and maximum sensitivities are reduced. Thus, r_e can be appropriately reduced to improve the sensitivity.

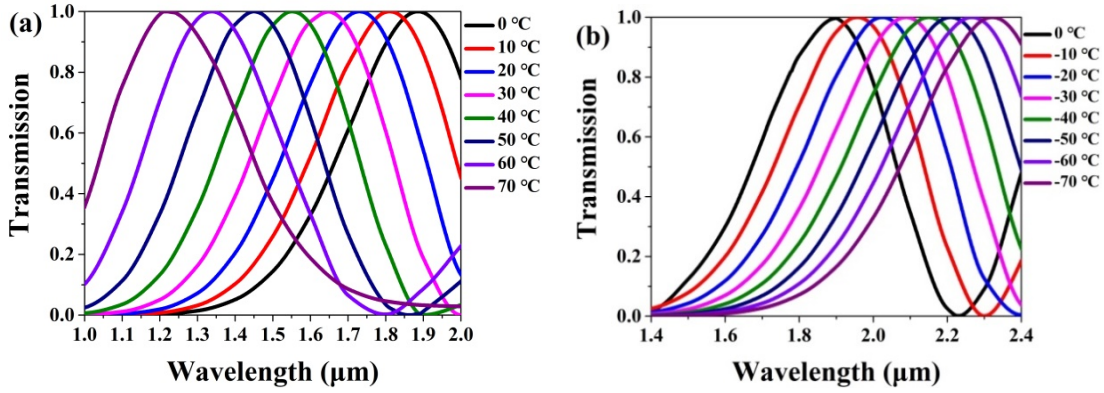

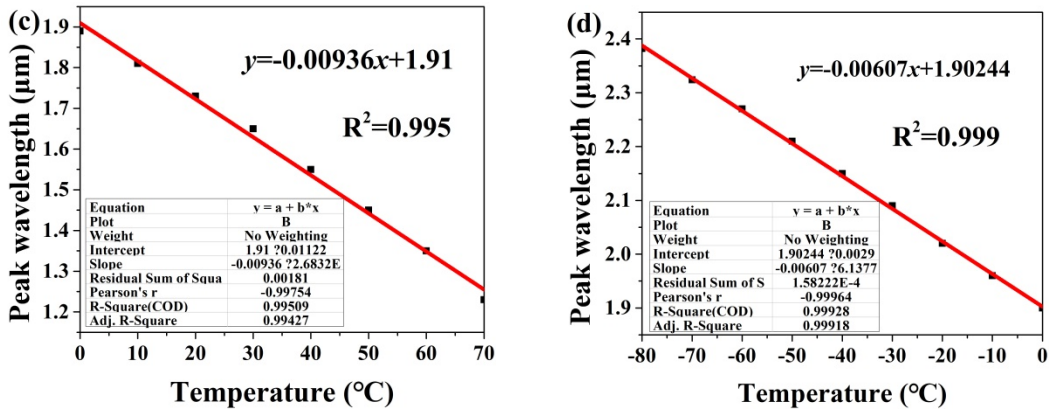

Fig. 7. The transmission spectra of the *x*-polarized light at different temperature ranges from (a) 0 to 70 ℃ and (b) -80 to 0 ℃, respectively, when L=1.7 mm. The variation in the peak wavelengths and linear fitting results when the temperature changes from (c) 0 to 70 ℃ and (d) -80 to 0 ℃, respectively.

Fig. 7(a) shows the transmission spectra of the *x*-polarized light in the temperature range of 0 to 70 ℃ when L=1.7 mm. From Fig. 7(a), when L increases from 1.5 to 1.7 mm, the peak wavelengths at the same temperature occur to blue-shift. Fig. 7(b) shows the transmission spectra of the *x*-polarized light in the temperature range of -80 to 0 ℃ when L=1.7 mm. From Fig. 7(b), when L increases from 1.5 to 1.7 mm, the peak wavelengths at the same temperature also occur to blue-shift. It can be known from Eq. (4) that compared to other structure parameters, the effective refractive indices of the supermodes cannot be changed by L. Thus, L_c will not be changed when L increases. However, according to Eq. (6), P_B transfers from the core A to B, and L shows the quadratic relationship of the sine function. Thus, when L increases, the peak wavelengths at the same temperature occur to blue-shift. Figs. 7(c) and 7(d) show the variation in the peak wavelengths and linear fitting results when the temperature changes from 0 to 70 ℃ and -80 to 0 ℃, respectively. From Fig. 7(c), the linear fitting result is y=-0.00936x+1.91, R^2 is 0.995, the average sensitivity is -9.36 nm/℃, and the maximum sensitivity can achieve -13.0 nm/℃ in the temperature range of 60 to 70 ℃. From Fig. 7(d), the linear fitting result is y=-0.00607x+1.90244, R^2 is 0.999, the average sensitivity is -6.07 nm/℃, and the maximum sensitivity can achieve -6.0 nm/℃ in the temperature range of 0 to -20 ℃. It is found that even if L is increased by 0.2 mm, the temperature sensitivity is changed slightly.

4. Discussion

Based on the above analyses, we optimize the fiber structure parameters as r_t=1.41 μm, Λ=3.72 μm, r_e=0.30 μm, and r_f=0.65 μm. n_f-n_{silica}=-0.008, and L=1.6 mm. At this time, the transmission spectra of the *x*-polarized light in the temperature ranges of 0 to 70 ℃ and -80 to 0 ℃ are shown in Figs. 8(a) and 8(b).

It can be seen from Figs. 8(a) and 8(b) the peak wavelengths occur to blue-shift with the increase of the temperature. Figs. 8(c) and 8(d) show the variation in the peak wavelengths and linear fitting results when the temperature changes from 0 to 70 ℃ and -80 to 0 ℃. From Fig. 8(c), the linear fitting result is y=-0.01164x+2.1425, the average temperature sensitivity is -11.64 nm/℃, and the maximum sensitivity can achieve -15.0 nm/℃ in the temperature range of 60 to 70 ℃. From Fig. 8(d), the linear fitting result is y=-0.00741x+2.12644, the average temperature sensitivity is -7.41 nm/℃, and the maximum sensitivity can achieve -9.0 nm/℃ in the temperature range of -10 to 0 ℃. In addition, the high R^2 values indicate that the good linearity are obtained for the temperature sensing sensitivity.

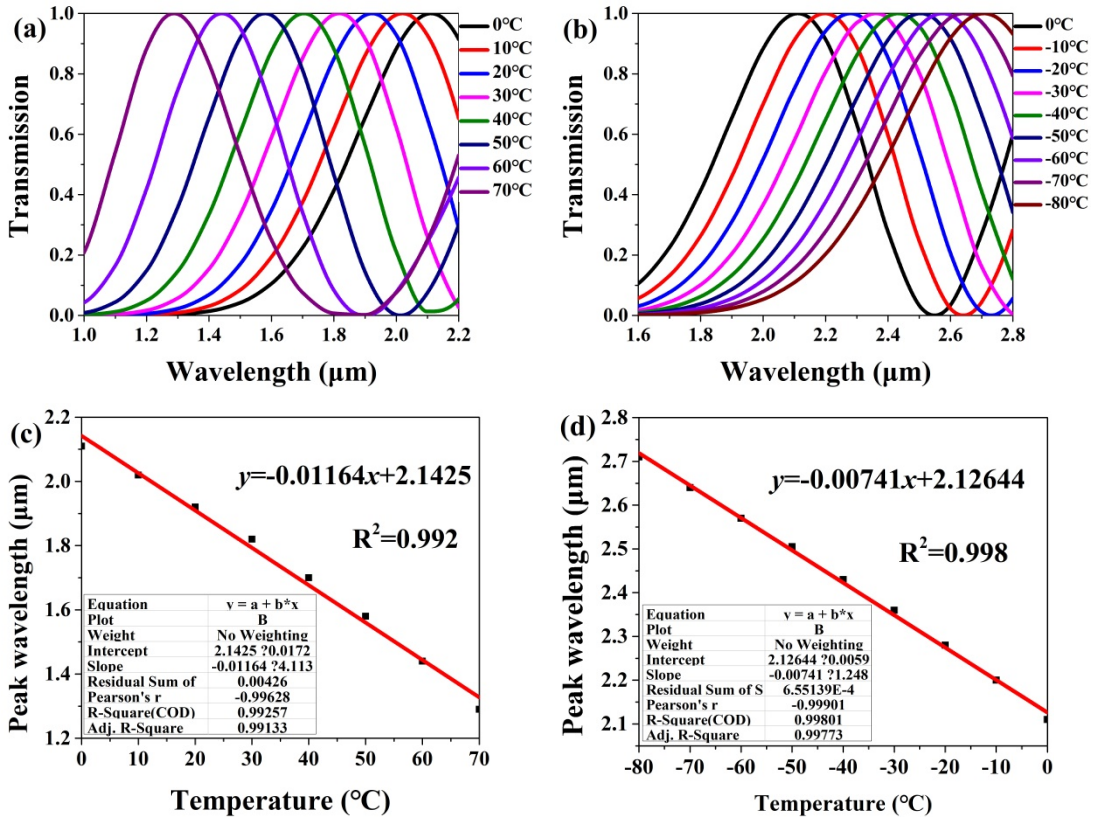

Fig. 8. The transmission spectra of the *x*-polarized light with different temperature ranges from (a) 0 to 70℃ and (b) -80 to 0℃, respectively, when the fiber structure parameters are optimized. The variation in the peak wavelengths and linear fitting results when the temperature changes from (c) 0 to 70℃ and (d) -80 to 0℃, respectively.

The influence of the hydrostatic pressure on the temperature sensing is also investigated. According to the photoelastic effect, n_{silica}, which is modulated by the hydrostatic pressure, can be described as [29]:

$$\begin{aligned} n_x &= n_{\text{silica}} - C_1\sigma_x - C_2(\sigma_y + \sigma_z), \\ n_y &= n_{\text{silica}} - C_1\sigma_y - C_2(\sigma_x + \sigma_z), \\ n_z &= n_{\text{silica}} - C_1\sigma_z - C_2(\sigma_x + \sigma_y), \end{aligned} \tag{8}$$

where σ_x, σ_y, and σ_z are the pressure components. In this work, the Yong's modulus E_{silica}=73.1Gpa, and Poisson's ratio υ_{silica} is set as 0.17. C_1=6.5×10^{-13} m^2/N, and C_2=4.2×10^{-12} m^2/N [30, 31]. Because of the all-solid cladding structure, the proposed DC-PCF is pressure resistant.

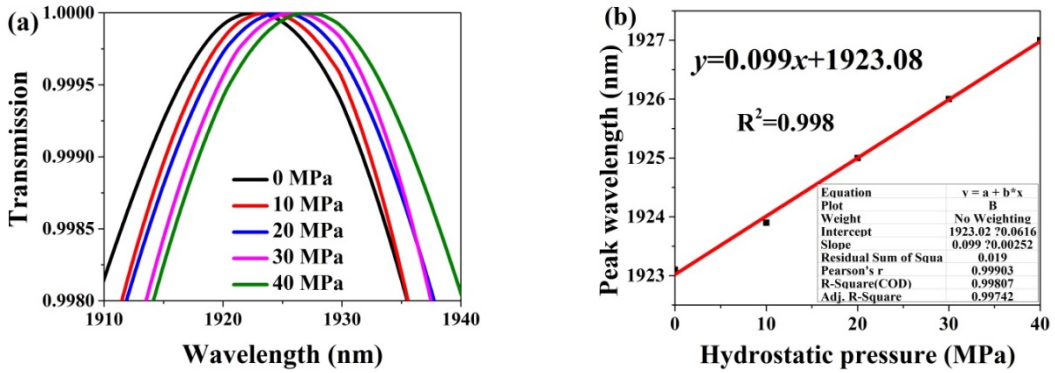

Fig. 9. (a) The variation in the peak wavelengths, and (b) the linear fitting results when the hydrostatic pressure changes from 0 to 40 Mpa.

Figs. 9(a) and 9(b) show the variation in the peak wavelengths and linear fitting results when the

hydrostatic pressure changes from 0 to 40 Mpa at the temperature of 20 °C. From Fig. 9(a), as the hydrostatic pressure increases, the peak wavelengths slightly occur to red-shift. The all-solid cladding makes the proposed DC-PCF stronger and less sensitive to the hydrostatic pressure compared to the air-silica PCFs. Compared with the peak wavelengths shift induced by the temperature, the effect of the hydrostatic pressure is almost negligible. From Fig. 9(b), the linear fitting result is y=-0.099x+1923.08, and the average hydrostatic pressure sensitivity is only 0.099 nm/MPa. Thus, the proposed temperature sensor is insensitive to the hydrostatic pressure. The comparisons between the proposed all-solid cladding DC-PCF temperature sensing and other reports are shown in Table 1. It can be clearly seen from the Table 1 that the proposed temperature sensor has high temperature sensitivity and wide detection range. In addition, for the proposed all-solid cladding DC-PCF, only the three air holes need to be filled with the liquids, so the cladding deformation can be avoided, and the good performance of the temperature sensing can be achieved.

Table 1. Comparison between the proposed all-solid cladding DC-PCF temperature sensing with other reports.

Ref.	Structures	Temperature detection range (°C)	|Sensitivity| (nm/°C)
[9]	Ethanol-Filled photonic bandgap fibers.	25-50	0.292
[10]	Toluene filled PCF.	-80-90	6.02
[11]	Oil-filled PCF.	30-150	0.61
[12]	Water-filled dual-core PCF.	30-70	0.818
[13]	Selectively gold-coated PCF.	0-50	0.72
[14]	SPR-based liquid-filled PCF.	0-100	3.08
[15]	SPR-based D-shaped PCF temperature sensor	20-50	3.635
This work	Dual-core toluene and ethanol filled PCF	0-70 -80-0	11.64 7.41

5. Fabrication and filling processes of the all-solid cladding DC-PCF

Fig. 10 shows the schematic diagram of the all-solid cladding DC-PCF fabrication with the stack and draw method. From Fig. 10, the capillary rods are first stacked in a regular hexagonal arrangement to obtain the desired structure, where the three hollow silica rods are placed in the center and the solid fluorine-doped silica rods are arranged in the cladding region. Then, the DC-PCF preform is formed by putting the arranged structure into a silica glass tube. After that, the DC-PCF cane is obtained by drawing the preform under the optimized parameters of the drawing tower. Finally, the jacket tube is added to the surface of the DC-PCF to obtain the desired DC-PCF.

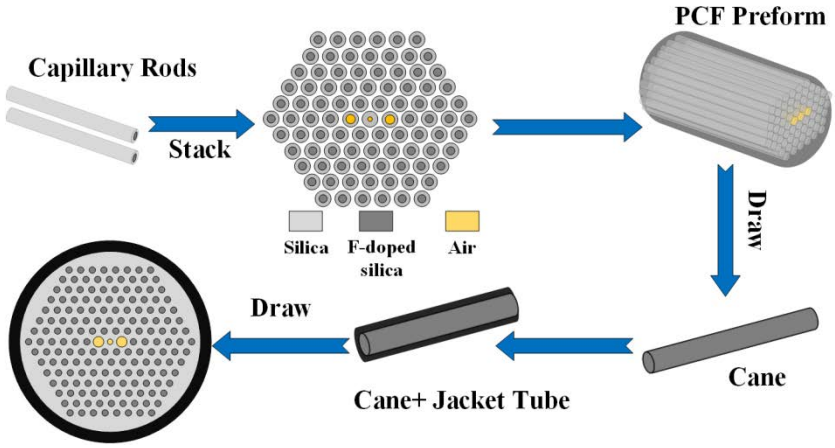

Fig. 10. The schematic diagram of the all-solid cladding DC-PCF fabrication with the stack and draw method.

Selectively filling the toluene and ethanol into the air holes can be achieved by the multi-step filling technique [32-34]. Fig. 11 shows the schematic diagram of the all-solid cladding DC-PCF filling with the multi-step filling technique. First, a section of all-solid cladding DC-PCF with the length of ~10 cm is taken, and then the UV glue carried by the mental tip can be aligned with the air holes of the target DC-PCF through adjusting the relative positions of the end face of the DC-PCF and the UV glue droplets. Second, a UV lamp is used to irradiate the end face of the DC-PCF until the UV glue is completely cured. Third, the end face of the DC-PCF is inserted into the toluene, and a gas pump is used to pump the toluene into the two air holes. Fourth, the length of the central air hole sealed by UV glue is cut off, and then the first and second steps are reused to seal the two air holes filled with the toluene. After that, the same method can be used to fill the central air hole with the ethanol. Finally, the desired fiber length can be obtained by cutting off the all-solid cladding DC-PCF filled with the toluene and ethanol.

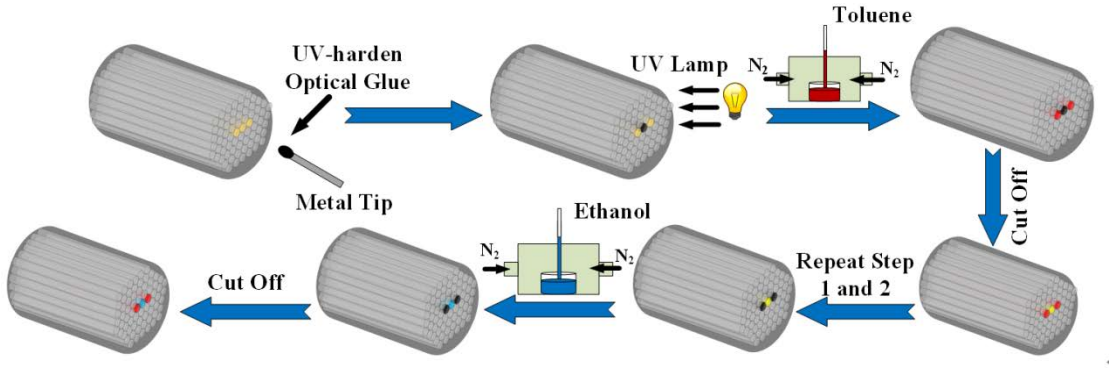

Fig.11. The schematic diagram of the all-solid cladding DC-PCF filling with the multi-step filling technique.

6. Conclusion

In summary, an all-solid cladding DC-PCF filled with the toluene and ethanol is proposed for the temperature sensing. The two cores of the DC-PCF are filled with the toluene, and the central air hole is filled with the ethanol. By optimizing the fiber structure parameters, the average temperature sensitivity can achieve -11.64 and -7.41 nm/°C in the temperature ranges of 0 to 70 °C and -80 to 0 °C, respectively. The maximum temperature sensitivity in the two temperature ranges can achieve -15 and -9 nm/°C, respectively. Moreover, the average hydrostatic pressure sensitivity is only -0.099 nm/MPa, so the proposed temperature sensor based on the all-solid cladding DC-PCF is insensitive to the hydrostatic

pressure.

Acknowledgments

This work is supported by National Key Research and Development Project of China (Granted Nos. 2019YFB2204001) and the National Natural Science Foundation of China (Granted Nos. 61875238 and 61935007).

References

[1] P. Marć, N. Przybysz, A. Molska, L.R. Jaroszewicz . Photonic Crystal Fiber Transducers for an Optical Fiber Multilevel Temperature Threshold Sensor [J]. J Lightwave Technol, 36(4) (2018) 898 – 903.

[2] A.K. Paul, A.K. Sarkar, A. B. S. Rahman, A. Khaleque. Twin Core Photonic Crystal Fiber Plasmonic Refractive Index Sensor [J]. IEEE Sens. J, 18(14) (2018) 5761 - 5769.

[3] M. De, V.K. Singh, Magnetic fluid infiltrated dual core photonic crystal fiber based highly sensitive magnetic field sensor [J]. Opt. Laser Technol, 106 (2018) 61-68.

[4] J.Y. Huang, J.V. Roosbroeck, J. Vlekken, A.B. Martinez, T. Geernaert, F. Berghmans, B.V. Hoe, E. Lindner, C. Caucheteur. FBGs written in specialty fiber for high pressure/high temperature measurement [J]. Opt. Express, 25(15) (2017) 17936.

[5] S.M. Kuo, Y.W. Huang, S.M. Yeh, W.H. Cheng, C.H. Lin. Liquid crystal modified photonic crystal fiber (LC-PCF) fabricated with an SU-8 photoresist sealing technique for electrical flux measurement [J]. Opt. Express, 19(19) (2011) 18372-18379.

[6] Y. Li, Y. Liu, D. Luo. Optical thermal sensor based on cholesteric film refilled with mixture of toluene and ethanol [J]. Opt. Express, 25(21) (2017) 26349-26355.

[7] J.L. Vilas, J.A. Sanchez-Martin, E. Bernabeu. Temperature dependence of birefringence in ethanol-filled suspended core fiber [J]. Appl. Opt, 55(23) (2016) 6222-6228.

[8] M. Lu, X. Zhang, Y. Liang, L. Li, J.F. Masson, W. Peng. Liquid crystal filled surface plasmon resonance thermometer [J]. Opt. Express, 24(10) (2016) 10904-10911.

[9] B. Dong, Z. Shen, C. Yu, Y. Wang. Modal excitations in fully and partially ethanol-filled photonic bandgap fibers and their applications as fiber sensors [J]. J Lightwave Technol, 34(16) (2016)

[10] J. Ma, H. Yu, X. Jiang, D. Jiang. High-performance temperature sensing using a selectively filled solid-core photonic crystal fiber with a central air-bore [J]. Opt. Express, 25(8) (2017) 9406-9415.

[11] Y. Geng, L. Wang, X. Tan, Y. Xu, X. Hong, X. Li. A Compact Four-Wave Mixing-based Temperature Fiber Sensor with Partially Filled Photonic Crystal Fiber [J]. IEEE Sens. J, 19(8) (2019) 2956-2961.

[12] M.S. Alam, S. Akter, B.K. Paul, K. Ahmed, D. Vigneswaran, M.N. Aktar. FEM based highly sensitive dual core temperature sensor: design and analysis [J]. OSA Continuum, 2(9) (2019) 2581-2592.

[13] Y. Peng, J. Hou, Z. Huang, Q. Lu. Temperature sensor based on surface plasmon resonance within selectively coated photonic crystal fiber[J]. Appl. Opt, 51(26) (2012)6361-6367.

[14] C. Liu, F. Wang, J. Lv, T. Sun, Q. Liu, C. Fu, H. Mu, P. K. Chu. A highly temperature-sensitive photonic crystal fiber based on surface plasmon resonance[J]. Opt. Commun, 359 (2016) 378-382.

[15] S. Weng, L. Pei, J. Wang, T. Ning, J. Li. High sensitivity D-shaped hole fiber temperature sensor based on surface plasmon resonance with liquid filling[J]. Photonics Res, 5(2) (2017)103-107.

[16] M. Klimczak, B. Siwicki, P. Skibiński, D. Pysz, R. Stępień, A. Heidt, C. Radzewicz, R. Buczyński. Coherent supercontinuum generation up to 2.3 μm in all-solid soft-glass photonic crystal fibers with

flat all-normal dispersion[J].Opt. Express, 22(15) (2014)18824-18832.
[17] M. Klimczak, B. Siwicki, B. Zhou, M. Bache, D. Pysz, O. Bang, R. Buczyński, Coherent supercontinuum bandwidth limitations under femtosecond pumping at 2 μm in all-solid soft glass photonic crystal fibers, Opt. Express 24(26) (2016) 29406-29416.
[18] G. Ghosh, M. Endo, T. Iwasaki. Temperature-dependent Sellmeier coefficients and chromatic dispersions for some optical fiber glasses [J]. J Lightwave Technol,12(8) (1994)1338-1342.
[19] T. Wu, Y. Liu, Z. Yu, Y. Peng, C. Shu, H Ye. The sensing characteristics of plasmonic waveguide with a ring resonator [J]. Opt. Express, 22(7) (2014) 7669-7677.
[20] E. Sani, A, Dell'Oro. Spectral optical constants of ethanol and isopropanol from ultraviolet to far infrared [J]. Optical Mater, 60 (2016) 137-141.
[21] T. Wu, Y. Liu, Z. Yu, H. Ye, Y. Peng, C. Shu, C.Yang, W. Zhang, H. He. A nanometeric temperature sensor based on plasmonic waveguide with an ethanol-sealed rectangular cavity [J]. Opt. Commun, 339 (2015) 1-6.
[22] K. Saitoh, Y. Sato, M. Koshiba. Coupling characteristics of dual-core photonic crystal fiber couplers [J].Opt. Express, 11(24) (2003) 3188–3195.
[23] L. Jiang, Y. Zheng, L. Hou, K. Zheng, J. Peng, X. Zhao. A novel ultra-broadband single polarization single mode photonic crystal fiber [J]. Opt. Commun, 396 (2017) 8-14.
[24] W.P. Huang. Coupled mode theory for optical waveguids: an overview [J]. Opt. Soc. Am. A ,11 (3) (1994) 963–983.
[25] J. Zi, S. Li, G. An, Z. Fan. Short-length polarization splitter based on dual-core photonic crystal fiber with hexagonal lattice [J]. Opt. Commun, 363(2016) 80-84.
[26] P. Madhavan, V. Thamizharasi, M.V.R. Kumar, A.Sampathkumare. A.S. Kumar, Md. A. Jabind, Numerical, Investigation of temperature dependent water infiltrated D-shaped dual core photonic crystal fiber (D-DC-PCF) for sensing applications [J]. Results Phys,13 (2019) 102289.
[27] X. Yang , Y. Lu , B. Liu, J. Yao. High Sensitivity Hollow Fiber Temperature Sensor Based on Surface Plasmon Resonance and Liquid Filling [J]. IEEE Photonics J, 10 (2) (2017)1-9.
[28] G. An, S. Li, X. Yan, X. Zhang, Z. Yuan, Y. Zhang, High-sensitivity and tunable refractive index sensor based on dual-core photonic crystal fiber, J. Opt. Soc. Am. B 33(7) (2016) 1330-1334.
[29] D. Chen, G. Hu, L. Chen. Dual-Core Photonic Crystal Fiber for Hydrostatic Pressure Sensing [J]. IEEE Photonic tech L, 23 (24) (2011) 1851-1853.
[30] M. Szpulak, T. Martynkien, W. Urbanczyk. Effects of hydrostatic pressure on phase and group modal birefringence in microstructured holey fibers [J]. Appl. Opt, 43(24) (2004) 4739-4744.
[31] Z. Liu, M.L.V Tse, C. Wu, D. Chen, C. Lu, H.Y. Tam. Intermodal coupling of supermodes in a twincore photonic crystal fiber and its application as a pressure sensor [J]. Opt. Express, 20(19) (2012) 21749-21757.
[32] B.T. Kuhlmey, B.J. Eggleton, D. Wu. Fluid-Filled Solid-Core Photonic Bandgap Fibers [J]. J Lightwave Technol, 27(11) (2009) 1617-1630.
[33] Y. Huang, Y. Wang, L. Zhang, Y. Shao, F. Zhang, C. Liao, Y. Wang. Tunable electro-optical modulator based on a photonic crystal fiber selectively filled with liquid crystal [J]. J Lightwave Technol, 37(9) (2019)1903-1908.
[34] Q. Liu , S. Li , X. Gao . Highly sensitive plasmonics temperature sensor based on photonic crystal fiber with a liquid core [J]. Opt. Commun, 427 (2018) 622-627.